ULTRA-SHARP ANGULAR FILTERING OF FAR-FIELD SIGNALS WITH GRADED-INDEX MULTILAYERS

by

Sanat Shukurov

A Thesis Submitted to the Faculty of the

DEPARTMENT OF PHYSICS

In Partial Fulfillment of the Requirements
For the Degree of

BACHELOR OF SCIENCE

In the School of Sciences and Humanities

NAZARBAYEV UNIVERSITY

2023

NAZARBAYEV UNIVERSITY, SCHOOL OF SCIENCES AND HUMANITIES

As members of the thesis committee, we certify that we have read the thesis prepared by Sanat Shukurov entitled

ULTRA-SHARP ANGULAR FILTERING OF FAR-FIELD SIGNALS WITH GRADED-INDEX MULTILAYERS

and recommend that it be accepted as fulfilling the thesis requirement for the degree of Bachelor of Science.

_____ Date: May 10, 2023

_____ Date: May 10, 2023

Final approval and acceptance of this thesis is contingent upon the candidate's submission of the final copies of the thesis to the Department of Physics.

I hereby certify that I have read this thesis prepared under my direction and recommend that it be accepted as fulfilling the thesis requirement.

_____ Date: May 10, 2023
Thesis Director: Constantinos Valagiannopoulos

ABSTRACT

Dielectric multilayers with graded index treat the propagating waves impinging at different angles very differently, due to total internal reflection. Such an ultra-sharp change in the response can be exploited for filtering, manipulation and tailoring of spatially distributed electromagnetic signals. Various utilities of the proposed filter such as power splitting, DC isolation, beam shifting and low-profile energy interaction are demonstrated, even in the presence of losses. The proposed setup can be vital as component in the operation of integrated photonic devices dealing with optical signal processing and analog information control.

PREFACE

I would like to express my sincerest gratitude to all peers and professors, who have helped me along the thorny path of completing this thesis. In particular, I thank my supervisor, Professor Constantinos Valagiannopoulos, for providing extensive feedback, support, and guidance during the entirety of this project.

I should also mention that the content of this thesis largely overlaps with the content of the article of the same title co-authored by me and Professor Valagiannopoulos. Unpublished at the time of submission of this thesis, the paper has been accepted for publication into a highly selective journal (Scopus 10%) dedicated to the advancements in the competitive discipline of Electrical and Electronic Engineering, "IEEE Transactions on Antennas and Propagation."

TABLE OF CONTENTS

1 INTRODUCTION

1.1 Demand for Photonic Devices

Structures that can transform the spatial distribution of the electromagnetic waves, like lenses, have been a major research objective of scientists for centuries. For instance, Maxwell himself has performed an extensive work on the formulation of generic laws governing the interaction of light with optical instruments [1]. Also, attempts to remedy the aberrations accompanying any image magnification by finite apertures have been recorded as early as 1948 [2]. In this regard, Luneburg was the first to capture the simple idea of changing the refractive index into a cylindrical or spherical domain so that all incoming rays have the same path length and get focused by exiting from the same point of the device [3]. Since then, no big research breakthrough occurred until the seminal works by Pendry reporting that the evanescent waves from a source can be restored at a distant target with use of negative refraction [4] and that suitably anisotropic media with inhomogeneous characteristics can control the electromagnetic fields within their volume [5]. Significant progress towards the wavefront engineering has been also made with help from epsilon-near-zero materials [6] and periodic placements of artificial particles that can impose any given law of diffraction via suitable phase shifts [7].

These and the related advances in the techniques of modulation of the incident fields have led to a number of fascinating applications. In particular, analog computing with spatially distributed signals has become feasible by utilization of subwavelength patterned screens [8], optimized inhomogeneous blocks surrounded by closed-loop networks [9] or platforms with tunable elements [10]. Importantly, on-chip architectures have been proposed based on an inversely designed silicon canvas that executes multiplexing [11], nanoslits of unequal length that perform focusing [12] and a cluster of dielectric nanoposts allowing for edge detection [13]. Moreover, it has been shown that free space can be substituted with nonlocal flat optical systems [14], while disordered scattering has been applied to improve resolution and bandwidth in imaging and communication [15]. Similarly, wavefront conversion is attainable with optimally loaded absorbing bilayers [16] and signal generation with arbitrary profile becomes feasible with quantum-dot-distributed feedback lasers [17]. Finally, neural networks are employed to design multilayered structures for temporal signal processing [18], while tensor impedance surfaces are used to build transformation electromagnetics devices [19].

In the aforementioned works, metamaterials have played a key role towards efficient implementation of blueprints created for the modification of electromagnetic signals. More recently, it has been demonstrated that setups composed of only two types of unit cells with different phase responses enable manipulation of waves in a programmable fashion [20], while two-dimensional plasma metamaterial devices allow for demultiplexing and waveguiding [21]. In addition, full control of optical transmission has been achieved via composite metascreens [22], ultrafast optical switching has been shown in polaritronic

metamaterials [23] and subwavelength resolution has been realized with metalenses in the visible spectrum [24]. Such a plethora of metamaterial-based designs has ignited sizable funding initiatives by significant players like Defense Advanced Research Projects Agency (DARPA) [25] and National Aeronautics and Space Administration (NASA) [26] for producing tunable optical filters in military and space applications. Large industrial interest has been also recorded towards the development of end-user metamaterial components for controlling electrodynamic signals by growing [27] and emerging [28] technology companies.

Metasurfaces, the two-dimensional siblings of metamaterials, are even more extensively utilized for the spatial manipulation of electromagnetic fields [29, 30] since they fit into a boundary without requiring bulky configurations. They can support useful functionalities such as determining the Fourier transform of signals that interact with spatially varying momentum [31] or evaluating second derivative across a plane [32]. Interestingly, high-efficiency dielectric metasurfaces can be employed for optical edge detection [33], retro-reflection incorporating space harmonics of different order [34] and independent control of beam characteristics (phase, amplitude) [35]. Furthermore, simple metasurfaces enable multifunctional processing of electromagnetic waves via two sets of vertically integrated polarization-filtering meta-atoms [36] and allow for giant directivity boost that mitigates interference in visible light communications [37].

1.2 Graded-Index Multilayers

In this thesis, I consider a graded-index planar multilayered layout positioned between a dense incoming medium and vacuum. In this way, a propagating incident wave can be either fully transmitted into air due to the smooth textural transition or perfectly reflected due to total internal reflection. As a result, an ultra-sharp filtering of the impinging light is performed based on the angle of propagation and can execute operations like DC component isolation, power splitting or beam shifting. A variation analysis of the filter selectivity with respect to the permittivity levels, number of layers, overall thickness and presence of losses is provided to identify the functional modes of the device by trading off the design parameters. Therefore, the proposed setup can be directly utilized as a piece of integrated photonic systems serving a wide range of purposes from wavefront manipulation and optical signal processing to angular switching and directional sensing.

It is important to stress that the considered structure is extensively used, even by standard textbooks [38], but for objectives different from the ones of this thesis. Namely, this work focuses on the previously unexplored applications of the graded index designs for angular filtering by employing the total internal reflection to switch abruptly the mode of operation. Additionally, the filtering efficiency is evaluated for a large number of parameters both in lossless and lossy cases. Finally, based on the filtering properties, some novel applications listed in the previous paragraph are proposed and examined.

2 PROBLEM FORMULATION

2.1 Design Description

The filter design is based upon the structure depicted in Fig. 1(a), where U layers of thickness d are filled with magnetically inert (permeability μ_0) materials of relative permittivities ε_u for $u = 1, \cdots, U$; the utilized Cartesian coordinate system (x, y, z) is also defined. For the dielectric constants, the following inequality holds: $\varepsilon > \varepsilon_1 > \varepsilon_2 > \cdots > \varepsilon_{U-1} > \varepsilon_U > 1$ indicating an almost linear drop of $\varepsilon(z)$ for increasing z, as shown in the bottom inset of Fig. 1(a). The layered configuration has an overall thickness denoted by $D \equiv Ud$ and is positioned between the dielectrically dense left half space ($z < 0$, permittivity $\varepsilon\varepsilon_0$) and the empty right half space ($z > D$) of unitary relative permittivity (vacuum constants (ε_0, μ_0)).

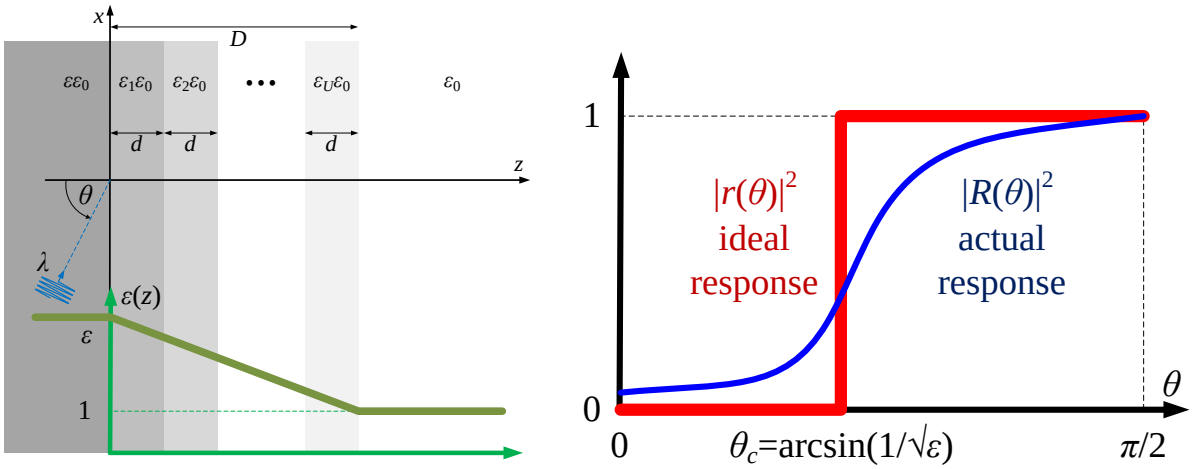

(a) (b)

Figure 1: (a) The physical configuration of the examined filtering setup. A layered structure of overall thickness D and U layers of the same size $d = D/U$, is obliquely illuminated by plane waves of wavelength λ traveling along directions that form various angles θ with the horizontal z axis. The permittivity $\varepsilon(z)$ drops with distance z, as shown in the bottom graph, from $\varepsilon > 1$ (corresponding to the dense left half space) to unity (corresponding to the empty right half space). (b) Sketch of the ideal $|r(\theta)|^2$ and the actual $|R(\theta)|^2$ reflectivity of the device as (even) functions of the angle θ, when high-pass filtering operation is desired. In the actual response, the permittivities may be considered as complex (lossy materials).

The setup is obliquely illuminated by plane waves characterized by the same wavelength λ of either TE (electric field E_y parallel to y axis, magnetic field $\mathbf{H}$ across zx plane) or TM type (magnetic field H_y parallel to y axis, electric field $\mathbf{E}$ across zx plane), that travel into vacuum along directions forming angles $-\pi/2 < \theta < \pi/2$ with the z axis. In order to treat the two polarizations with a unified notation, let us use the symbol F for both polarizations: it represents the only (y-directed) electric field component in the case of TE waves and the only magnetic component for TM waves.

For a moment, let us assume that the excitation is a plane wave incident at an angle θ. This is a strong assumption, but the Fourier analysis allows us to deduce the response to an arbitrary excitation using only the response to plane waves as will be discussed in more detail in the following section. Suppressing the time harmonic part of the form $e^{\mathrm{i}\omega t}$, the propagating plane wave is described by $F_{\mathrm{inc}}(z,x) = e^{-\mathrm{i}k(z\cos\theta + x\sin\theta)}$. When reflected, the plane wave will be modulated by a complex reflection coefficient $R(\theta)$, which can be analytically evaluated by employing the boundary conditions. The reflection coefficient, or rather reflectivity $|R(\theta)|^2$, is what determines the amount of energy carried by the reflected wave as dictated by Poyinting's theorem [38]. Thus, filtering out part of the spectrum is equivalent to constructing the system such that $|R(\theta)|^2 = 0$ for all angles in the undesired spectrum. This is demonstrated in fig. 1(b), where the reflectivity is plotted as a function of the angle of incidence θ. In the absence of losses ($\mathrm{Im}[\varepsilon(z)] = 0$) and for a very smooth permittivity transition ($D \to +\infty$ and $U \to +\infty$), the ideal response $|r(\theta)|^2$ is obtained. One can identify the critical total reflection angle $\theta_c = \arcsin(1/\sqrt{\varepsilon})$ beyond which the waves are purely evanescent into vacuum and thus 100% power reflection is recorded [39]. On the contrary, for $0 < \theta < \theta_c$, the reflections are negligible since the textural transition occurs across an extremely large distance (D) and with help from numerous (U) layers, each of which has permittivity almost equal to these of the neighboring layers. In a more realistic scenario where D is, at maximum, a few free-space wavelengths λ, one obtains the curve of actual response $|R(\theta)|^2$ which yields some reflections for $0 < \theta < \theta_c$ while absorbs a part of the incidence illumination for $\theta > \theta_c$, due to the inevitable losses. It should be stressed that, for a lossless design, one always obtains $|R(\theta)| = 1$ for $\theta > \theta_c$, regardless of the finite thickness D/λ. This thesis aims at providing multilayers that work as ultra-sharp, high-pass angular filters for the reflected beams, namely, photonic setups that reflect only the rapidly varying input signals being spatially distributed along x axis.

2.2 Analytical Solution

The famous Maxwell equations are a set of four partial differential equations that summarize the empirical laws describing the behavior of charged particles and electromagnetic fields. They are an essential tool for the design of photonic devices, which, by definition, employ the light-based phenomena to achieve the desired result. For the angular filter discussed in this work, it is sufficient to state the homogeneous Maxwell equations, which describe the electromagnetic fields in the absence of electric charges and currents [38]:

$$\boldsymbol{\nabla} \cdot \mathbf{E} = 0 \tag{1}$$

$$\boldsymbol{\nabla} \cdot \mathbf{H} = 0 \tag{2}$$

$$\boldsymbol{\nabla} \times \mathbf{E} = -\mu \frac{\partial \mathbf{H}}{\partial t} \tag{3}$$

$$\boldsymbol{\nabla} \times \mathbf{H} = \varepsilon \frac{\partial \mathbf{E}}{\partial t}. \tag{4}$$

Taking the curl of both sides of equations (3) and (4), allows one to decouple the Maxwell equations as follows:

$$\boldsymbol{\nabla}\times\boldsymbol{\nabla}\times\mathbf{E}=-\mu\boldsymbol{\nabla}\times\left(\frac{\partial\mathbf{H}}{\partial t}\right)=-\mu\frac{\partial}{\partial t}(\boldsymbol{\nabla}\times\mathbf{H})=-\mu\varepsilon\frac{\partial^2\mathbf{E}}{\partial t^2} \tag{5}$$

$$\boldsymbol{\nabla}\times\boldsymbol{\nabla}\times\mathbf{H}=\varepsilon\boldsymbol{\nabla}\times\left(\frac{\partial\mathbf{E}}{\partial t}\right)=\varepsilon\frac{\partial}{\partial t}(\boldsymbol{\nabla}\times\mathbf{E})=-\mu\varepsilon\frac{\partial^2\mathbf{H}}{\partial t^2}. \tag{6}$$

Now, using the definition of Laplacian of a vector field, $\nabla^2\mathbf{F}=\boldsymbol{\nabla}(\boldsymbol{\nabla}\cdot\mathbf{F})-\boldsymbol{\nabla}\times\boldsymbol{\nabla}\times\mathbf{F}$, one arrives at the wave equations:

$$\nabla^2\mathbf{E}=\mu\varepsilon\frac{\partial^2\mathbf{E}}{\partial t^2} \tag{7}$$

$$\nabla^2\mathbf{H}=\mu\varepsilon\frac{\partial^2\mathbf{H}}{\partial t^2}, \tag{8}$$

where equations (1) and (2) were used. As usual, equations (7) and (8) can be converted into the scalar wave equations by imposing that the direction of the fields is given by a unit vector normal to the wavevector. Among many solutions of the scalar wave equations, the set of time harmonic plane waves $\{e^{\mathrm{i}\omega t\pm\mathrm{i}\boldsymbol{\beta}\cdot\mathbf{r}}:|\boldsymbol{\beta}|^2=\omega^2\mu\varepsilon\}$ can be shown to form a basis for the Hilbert space of solutions. As follows from the Fourier analysis, this allows us to write any solution as a weighted superposition of the plane waves. In general, the superposition would be expressed as a multiple integral, but, from the constraint $|\boldsymbol{\beta}|^2=\omega^2\mu\varepsilon$ and the symmetry of the setup depicted in Fig. 1(a), one can infer that the integral will be over only one independent component of the phase vector $\boldsymbol{\beta}$, namely, β_x. Then, β_z can be expressed as $\beta_z=\sqrt{\omega^2\mu\varepsilon-\beta_x^2}$. Since the system is stationary, let us omit the time harmonic part of the solution in the remaining sections.

With this, an arbitrary excitation can be written in the form:

$$F_{\mathrm{inc}}(z,x)=\int_{-\infty}^{\infty}A(\beta_x)e^{-\mathrm{i}(\beta_z z+\beta_x x)}\mathrm{d}\beta_x, \tag{9}$$

where $A(\beta_x)$ - complex amplitude of the plane wave with the corresponding phase. Note that, β_z can become complex; the plane waves with the phase satisfying $\beta_x^2\geq\omega^2\mu\varepsilon$ represent the evanescent part of the spectrum and they decay exponentially with increasing z. This fact allows to neglect the evanescent waves if the device is sufficiently far away from the source of excitation, so the boundaries of the Fourier integral would cover only the far-field spectrum. Then, the phase constants β_x and β_z can be associated with the angle of incidence of the plane wave, θ, and the wave number into the denser medium, $k\equiv k_0\sqrt{\varepsilon}=2\pi\sqrt{\varepsilon}/\lambda$, through the relation $\beta_x=k\cos\theta$ and $\beta_z=k\sin\theta$, respectively. Under the far-field approximation, the Fourier integral for the incoming signal becomes:

$$F_{\mathrm{inc}}(z,x)=\int_{-\pi/2}^{\pi/2}A(\theta)e^{-\mathrm{i}k(z\cos\theta+x\sin\theta)}\mathrm{d}\theta. \tag{10}$$

It should be stressed that $A(\beta_x)\neq A(\theta)$, but rather $A(\beta_x)\mathrm{d}\beta_x=A(\theta)\mathrm{d}\theta$. In other words, $A(\beta_x)$ and $A(\theta)$ are different functions that perform a similar role - they are amplitudes of

the corresponding plane wave - hence, why they are denoted by the same symbol. While somewhat confusing, this notation is very common in both Fourier optics and other fields of physics. In parallel with (10), the reflected ($z < 0$) field can be expressed as:

$$F_{\text{ref}}(z, x) = \int_{-\pi/2}^{\pi/2} A(\theta) R(\theta) e^{-\mathrm{i}k(-z\cos\theta + x\sin\theta)} \mathrm{d}\theta, \tag{11}$$

where the complex $R(\theta)$ is the reflection coefficient for the respective wave polarization that was mentioned in the previous section when the ideal response of the filter was discussed; it is an even function of θ due to the symmetry of the configuration with respect to z axis. Here, we can see the power of the Fourier optics: it allows to deduce the response of the system to an arbitrary excitation from the response to plane waves incident at different angles θ. In direct analogy to (11), the field in all the other regions can be written in the form:

$$F(z, x) = \int_{-\pi/2}^{\pi/2} A(\theta) f(z, \theta) e^{-\mathrm{i}kx\sin\theta} \mathrm{d}\theta. \tag{12}$$

The kernel $f(z, \theta)$ of (12) equals to $f_u(z, \theta) = T_u(\theta) e^{-\mathrm{i}\beta_u z} + R_u(\theta) e^{+\mathrm{i}\beta_u z}$ for $(u-1)d < z < ud$, into the u-th layer and $f_{\text{tran}}(z, \theta) = T(\theta) e^{-\mathrm{i}\beta_U (z-D)}$ for $z > D$, into the vacuum half space. Similarly to β_z in the incidence medium, for $(u-1)d < z < ud$, the quantity $\beta_u = k\sqrt{\varepsilon_u/\varepsilon - \sin^2\theta}$ is the spatial frequency associated with the z-direction; it becomes imaginary when the incidence angle θ exceeds the local critical angle.

The only unknowns in $f(z, \theta)$ are the coefficients $T_u(\theta)$ and $R_u(\theta)$ (or just $T(\theta)$ and $R(\theta)$ in the rightmost and leftmost semi-infinite layers respectively). This unknowns can be found analytically by employing the appropriate boundary conditions derived from the Maxwell equations (3) and (4) in their integral form [38]:

$$\oint_C \mathbf{E} \cdot \mathrm{d}\mathbf{l} = -\mu \frac{\mathrm{d}}{\mathrm{d}t} \iint_S \mathbf{H} \cdot \mathrm{d}\mathbf{s} \tag{13}$$

$$\oint_C \mathbf{H} \cdot \mathrm{d}\mathbf{l} = 0, \tag{14}$$

where the integrals are taken either over some closed curve C or the surface S enclosed by the curve. By considering progressively smaller rectangular boxes whose boundary is C and area is S, one can see that the value of the surface integral becomes negligible. If the box encloses some interface, one can see that the contribution of the line integral along the sides perpendicular to the interface will also be negligible (for a more detailed derivation, see [38]). Then, the integrals become:

$$\hat{\mathbf{n}} \times (\mathbf{E}_2 - \mathbf{E}_1) = 0 \tag{15}$$

$$\hat{\mathbf{n}} \times (\mathbf{H}_2 - \mathbf{H}_1) = 0, \tag{16}$$

where $\hat{\mathbf{n}}$ - unit vector normal to the interface and subscripts 1 and 2 denote the fields on the corresponding side of the interface. Finally, the unknown reflection and transmission

coefficients can be determined by imposing the necessary magnetic and electric boundary conditions (15) and (16) at every single interface $z = ud$ for $u = 0, \cdots, U$. Such a process generates $2(U + 1)$ linear equations which, by eliminating the intermediate coefficients, yield to the following 2×2 linear system with respect to the overall reflection $R(\theta)$ and transmission $T(\theta)$ coefficients.

$$\begin{bmatrix} R(\theta) \\ 1 \end{bmatrix} = \left\{ \mathbf{M} \cdot \left(\prod_{u=1}^{U-1} \mathbf{M}_u \right) \cdot \mathbf{v} \right\} T(\theta). \tag{17}$$

The symbol $\mathbf{M}_u$ is used for the 2×2 matrix representing the boundary conditions at $z = ud$ for $u = 1, \cdots, (U - 1)$ and written as:

$$\mathbf{M}_u = \begin{bmatrix} \frac{1+\gamma_u}{2} e^{+\mathrm{i}ud(\beta_{u+1}-\beta_u)} & \frac{1-\gamma_u}{2} e^{-\mathrm{i}ud(\beta_{u+1}+\beta_u)} \\ \frac{1-\gamma_u}{2} e^{+\mathrm{i}ud(\beta_{u+1}+\beta_u)} & \frac{1+\gamma_u}{2} e^{-\mathrm{i}ud(\beta_{u+1}-\beta_u)} \end{bmatrix}, \tag{18}$$

where $\gamma_u = \frac{\beta_{u+1}}{\beta_u}$ for TE waves and $\gamma_u = \frac{\varepsilon_u \beta_{u+1}}{\varepsilon_{u+1} \beta_u}$ for TM waves. $\mathbf{M}$ is the 2×2 matrix representing the boundary conditions at $z = 0$ and takes the form:

$$\mathbf{M} = \frac{1}{2} \begin{bmatrix} 1+\gamma \frac{\beta_1}{k \cos\theta} & 1-\gamma \frac{\beta_1}{k \cos\theta} \\ 1-\gamma \frac{\beta_1}{k \cos\theta} & 1+\gamma \frac{\beta_1}{k \cos\theta} \end{bmatrix}, \tag{19}$$

where $\gamma = 1$ for TE waves and $\gamma = \varepsilon/\varepsilon_1$ for TM waves. The 2×1 vector $\mathbf{v}$ concerns the imposed regimes at $z = Ud = D$ and is written as:

$$\mathbf{v} = \frac{1}{2} \begin{bmatrix} e^{-\mathrm{i}Ud\beta_U} \left(1 - \gamma_U\right) \\ e^{+\mathrm{i}Ud\beta_U} \left(1 + \gamma_U\right) \end{bmatrix}, \tag{20}$$

where γ_u can be defined also for $u = U$ with $\varepsilon_{U+1} = 1$. Note that the intermediate coefficients $T_u(\theta)$ and $R_u(\theta)$ for $u = 1, \cdots, U$ can be determined from the overall reflection $R(\theta)$ and transmission $T(\theta)$ of (17), by employing the suitable transfer matrices [40].

As indicated in Fig. 1(b), even in the absence of losses, the actual response of the system ($|R(\theta)|^2$) will differ from the ideal response ($|r(\theta)|^2$) due to textural transitions in the multilayered system. To assess this difference for a given set of parameters, the following metric is introduced:

$$\rho = \left\{ \frac{1}{2\theta_c} \int_0^{\theta_c} + \frac{1}{\pi - 2\theta_c} \int_{\theta_c}^{\pi/2} \right\} \left| |R(\theta)|^2 - |r(\theta)|^2 \right| \mathrm{d}\theta. \tag{21}$$

Two integrals with different weights are used to prevent the metric from spuriously favoring lossless systems ($|R(\theta)| = |r(\theta)| = 1$ for $\theta > \theta_c$) with small critical angles θ_c. The sum of two integrals is divided by two for normalization; thus, $\rho = 1$ in the worst-case scenario of a structure being totally transparent for $\theta > \theta_c$ and behaving as impenetrable screen for $\theta < \theta_c$.

3 NUMERICAL RESULTS

3.1 Proof of Concept

To demonstrate the operation of the proposed setup as an angular filter, it would be meaningful to represent the electromagnetic signal along the longitudinal axis passing normally through each layer. In Fig. 2(a), I assume TE fields and show the magnitude of the sole electric component $|F = E_y|$ with respect to z/λ for plane waves traveling along various incoming directions θ and with unitary magnitude. As anticipated, the incident beams at angles $\theta > \theta_c$ become evanescent when they find themselves into a layer of sufficiently sparse material with $\varepsilon_u < \varepsilon \sin^2\theta$. As a result, they have a vanishing transmissivity and, thus, reflect 100% (in the lossless case) of the incident power and create standing-wave patterns. On the contrary, when less oblique waves are considered with $\theta < \theta_c$, the reflections are negligible and practically all the power is channeled into free space. Remarkably, as they pass through the filter, they fluctuate around an increasing, on average, magnitude. Indeed, higher electric fields are required to carry the same amount of energy in sparser dielectrics.

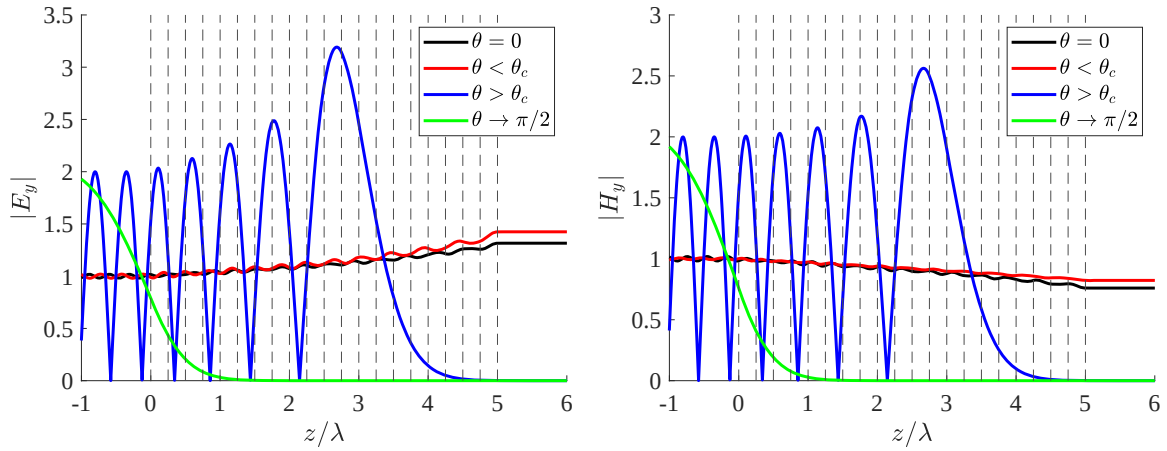

Figure 2: Magnitude of the sole field component as a function of longitudinal coordinate z/λ for various incidence angles θ, smaller or bigger than the critical one θ_c, in the scenario of: (a) TE waves, (b) TM waves. Vertical dashed lines denote boundaries of each layer. Incidence of unitary magnitude is considered. Plot parameters: $\varepsilon = 3$, $U = 20$, $D = 5\lambda$.

In Fig. 2(b), I assume TM waves and show the magnitude of the sole magnetic component $|F = H_y|$ with respect to z/λ. A similar behavior is recorded manifesting the operational switch between matching regimes ($\theta < \theta_c$) and perfectly reflecting regimes ($\theta > \theta_c$). Unlike Fig. 2(a), the sole component of the field when $\theta < \theta_c$ is decreasing with respect to z/λ, since the wave impedance is inversely proportional to $\sqrt{\varepsilon_u}$ and only one of the two waves (traveling along positive z), dominate into each layer.

3.2 Performance Variation

To study the efficiency of the considered device as an ultra-sharp angular filter, it is more instructive to evaluate the variation of the inverse metric (21), namely $1/\rho$, with respect to the basic parameters of the system. In Fig. 3(a), I assume TE waves and show the quantity $1/\rho$ across the map of number of layers U and overall optical thickness D/λ. Two completely different kinds of behavior are observed: in the upper-left triangle, the filtering score is low even when the optical thickness of the device is substantial, while across the rest of the contour plot, $1/\rho$ is high and increases significantly with the total size. The border between the two regions of Fig. 3(a) corresponds to filters with individual layers almost equal to half of the operational wavelength ($d \cong \lambda/2$). Once $d > \lambda/2$ (upper-left triangle), the response depends strongly on the developed Fabry-Perot resonances; indeed, even a filtering device with significant D/λ, may operate poorly due to constructive interference between the reflected waves. Once $d < \lambda/2$, the performance $1/\rho$ is enhanced when the setup is thicker (increased D/λ) and more finely chopped (increased U). As expected, when the textural contrast between the neighboring layers vanishes, the wave effectively travels in a locally homogeneous medium, resulting in very weak reflections (less than 1% in most points).

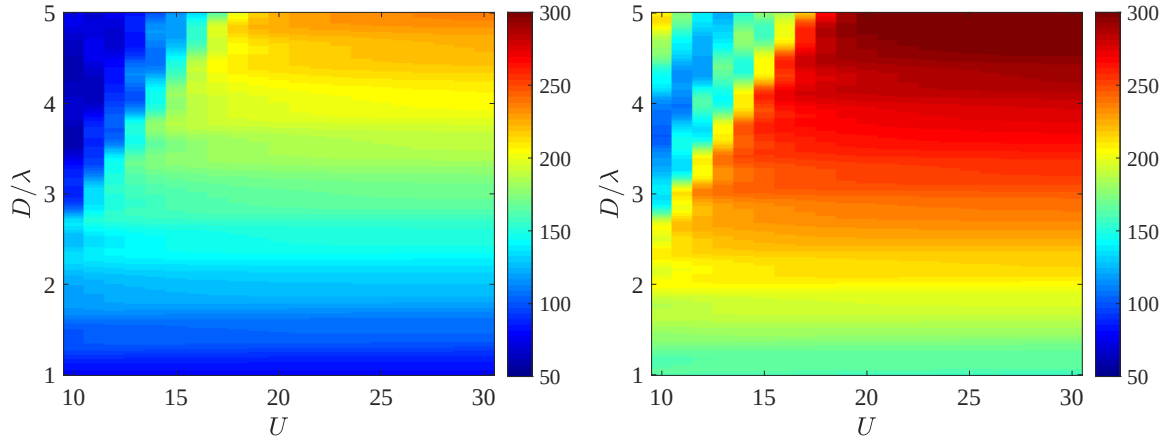

Figure 3: Performance $1/\rho$ as a function of the number of layers U and the total thickness of the device D/λ, in the cases of: (a) TE waves, (b) TM waves. Incidence of unitary magnitude is considered. Plot parameters: $\varepsilon = 3$.

In Fig. 3(b), I assume TM waves and repeat the calculations of Fig. 3(a); the two contour plots bear a close qualitative resemblance to each other. However, the filter works better in this scenario, namely, ρ is much smaller. The reason is that, for TM polarization, the electric field "feels" the permittivity gradient only with one of its two components, contrary to TE waves whose entire electric field vector is parallel to the interfaces and the reflections get relatively boosted. Note also the performance peak at the upper-left corner indicating a setup with reflected waves that interfere destructively so that only a small

portion of energy is reflected back. Finally, in both cases of Fig. 3, the score does not improve further by increasing the number of layers beyond a specific threshold since the permittivity transition is already quite smooth and the textural discretization becomes saturated.

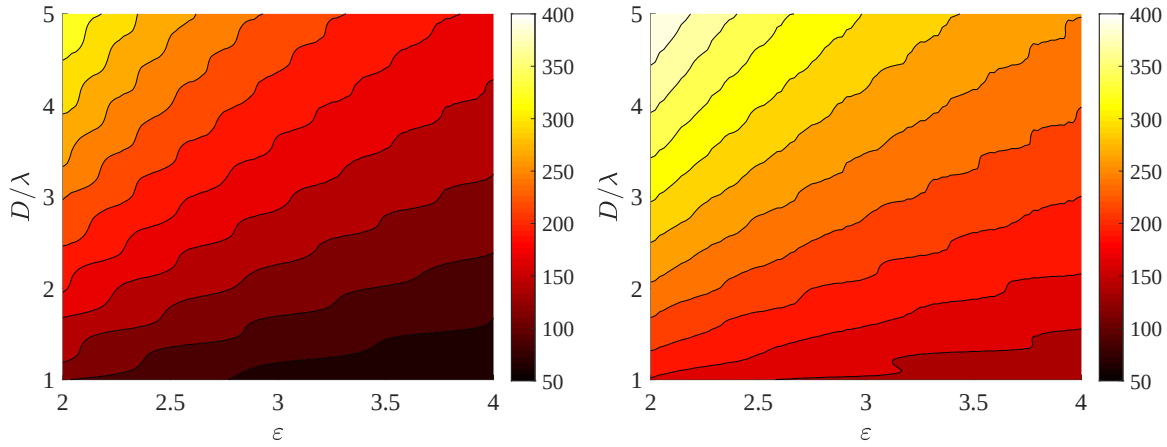

Figure 4: Performance $1/\rho$ as a function of the maximal permittivity ε and the total thickness of the device D/λ, in the cases of: (a) TE waves, (b) TM waves. Incidence of unitary magnitude is considered. Plot parameters: $U = 30$.

Furthermore, in Fig. 4(a), I consider TE waves and represent the quantity $1/\rho$ as a function of the maximal permittivity ε and the overall optical thickness D/λ. As expected, the filtering performance grows with total thickness, but gets smaller with the incidence permittivity. Indeed, as ε decreases, the leftmost medium becomes electrically sparser requiring less layers to reach its saturation limit. Similar qualitative conclusions hold for Fig. 4(b) dealing with TM fields, while, quantitatively, higher scores are spotted due to the nature of the developed waves, as indicated above.

3.3 Signals Filtering

To demonstrate the potential applications, it would be meaningful to see the response of the considered filter when fed by incoming signals with characteristic spatial distributions. In Fig. 5(a), I demonstrate how the proposed setup suppresses the DC component of the incoming illumination and reflects back only its harmonic part. Such a finding can be directly used in an integrated photonic system for the protection of sensitive equipment from large static intensity; it is rejected in the outer space and the operation continues with the oscillating signals. In particular, I impose at $z = 0$ a field given by $F_{\text{inc}} = 1 + \cos(\kappa x)$, with $k_0 < \kappa < k$ so that its spatial frequency κ is totally reflected, contrary to the DC offset which always passes through. Since the input is non-causal, the spatial Fourier transform of F_{inc} is a combination of three delta functions centered at $\theta = 0$ and $\theta_\kappa = \pm \arccos(\kappa/k)$, where θ_κ is the incidence angle of the wave constituting

the harmonic part of the input. Because $R(\theta)$ is an even function, the reflected signal takes the form: $F_{\text{ref}} = R(0) + R(\theta_\kappa)\cos(\kappa x)$, where $R(0)$ and $R(\theta_\kappa)$ are complex. In Fig. 5(a), I represent only the real parts of the waveforms and observe that the reflected component is a copy of the input signal shifted by the phase $\text{Arg}[R(\theta_\kappa)]$ and it fluctuates around zero instead of unitary level, since $R(0) \to 0$.

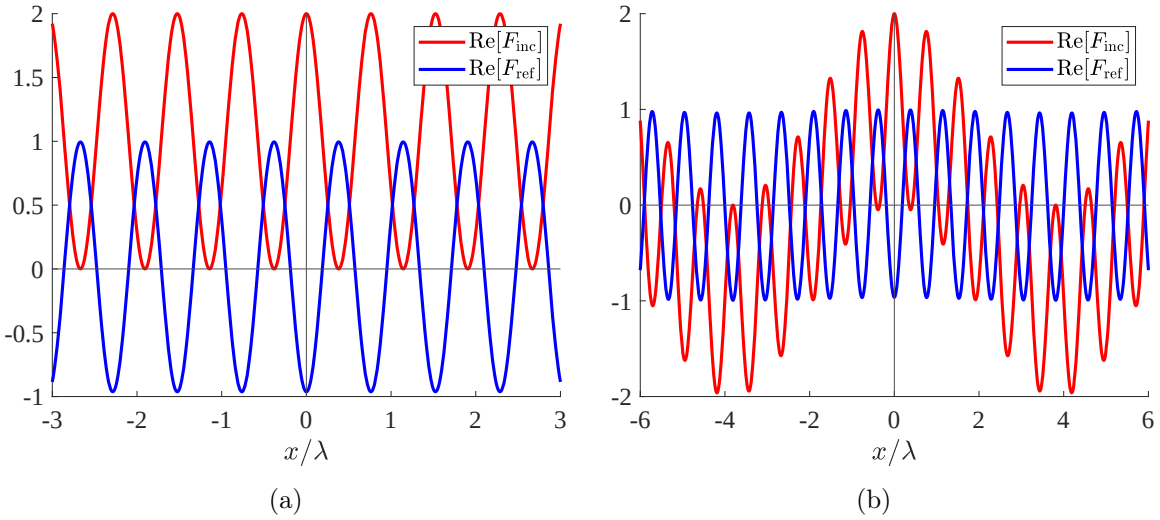

Figure 5: Spatial distribution of the real parts of the incident and reflected signals at $z = 0$ (TE polarization): (a) harmonic signal with a DC offset (DC isolator), (b) sum of two harmonic signals with large spatial frequency difference (power splitter). Plot parameters: $\varepsilon = 3$, $U = 20$, $D = 5\lambda$.

It is also instructive to see how the proposed filter responds to the input $F_{\text{inc}} = \cos(\kappa_1 x) + \cos(\kappa_2 x)$ comprising two harmonics (κ_1, κ_2). For such a signal, the output would be given by $F_{\text{ref}} = R(\theta_1)\cos(\kappa_1 x) + R(\theta_2)\cos(\kappa_2 x)$, where θ_1 and θ_2 are the respective incidence angles. Indeed, if I select the spatial frequencies such that $\kappa_1 < k_0 < \kappa_2 < k$, the reflection coefficients would satisfy $|R(\theta_1)| \ll |R(\theta_2)|$, meaning that only one of the two harmonics would be ultimately present. This is illustrated by Fig. 5(b), where I show how the real part of the reflected signal is just the tone with frequency κ_2, while the other harmonic, oscillating with κ_1, is filtered out. Since the two tones participate in the incoming signal with equal weights, the fact that only one of them is fully reflected means that the proposed device acts as a power splitter.

3.4 Beam Splitting

A more realistic input signal of finite power that may excite the device is the modulated Gaussian pulse written as:

$$F_{\text{inc}}(z = 0, x) = \sqrt[4]{\gamma\lambda^2}\, e^{-\gamma x^2} \cos(\kappa x). \tag{22}$$

The non-negative parameter γ controls how concentrated the pulse is and the factor $\sqrt[4]{\gamma\lambda^2}$ is added to normalize the signal in terms of the energy it carries; κ is, again, the frequency

of oscillations. The spatial Fourier transform of F_{inc} is a function of β_x and given by:

$$A(\beta_x) = \frac{1}{4\sqrt{\pi}\sqrt[4]{\gamma\lambda^2}} \left[e^{-\frac{(\beta_x+k)^2}{4\gamma}} + e^{-\frac{(\beta_x-k)^2}{4\gamma}} \right]. \tag{23}$$

As was mentioned before, the Fourier amplitudes in terms of the angle of incidence can be obtained using the relations $A(\beta_x)\mathrm{d}\beta_x = A(\theta)\mathrm{d}\theta$ and $\theta = \arccos(\beta_x/k) \Leftrightarrow \beta_x = k\cos\theta$.

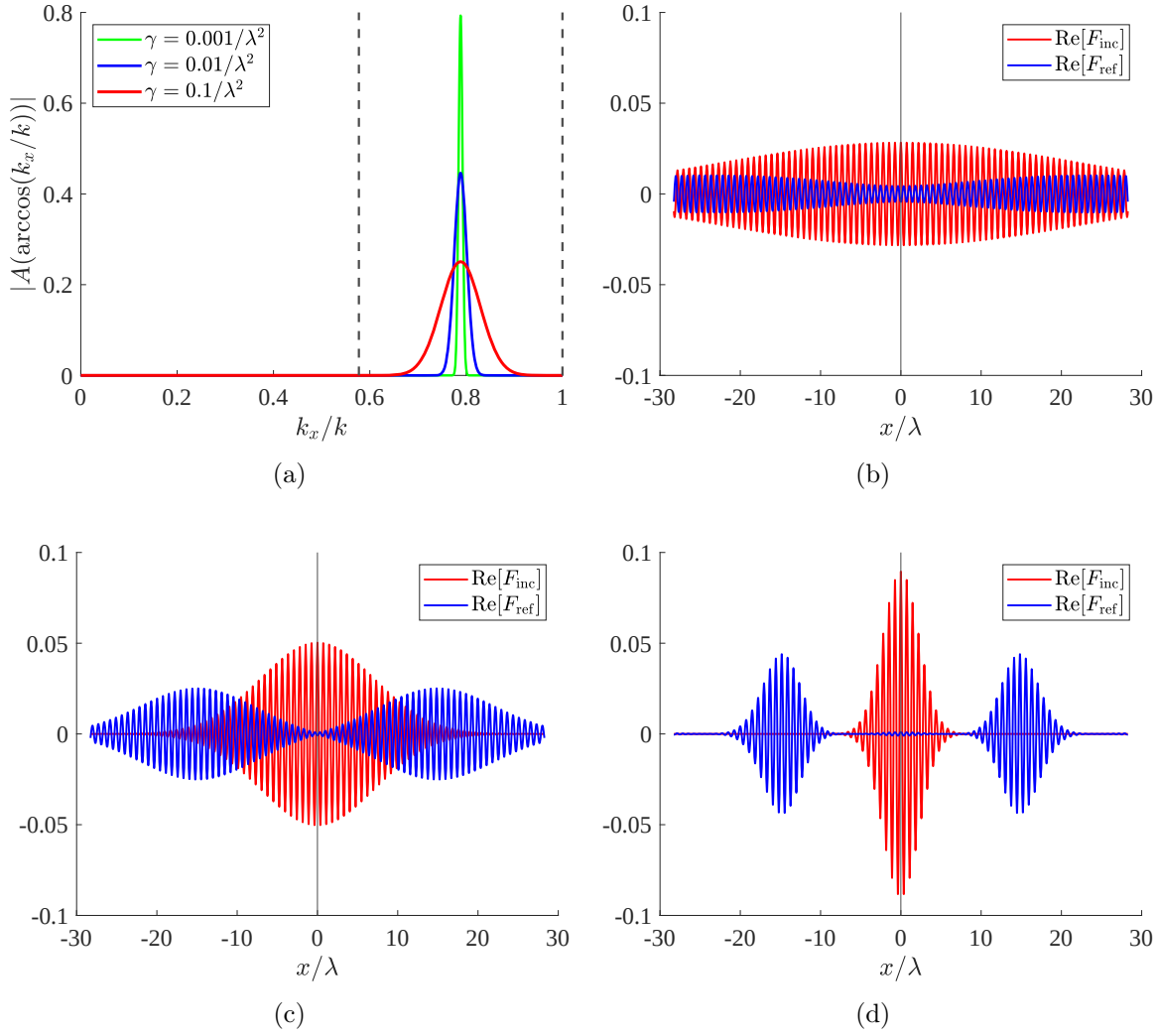

Figure 6: (a) Magnitude of spectral Fourier transform of modulated Gaussian pulses with different spread, but the same power, serving as incoming signals ($z = 0$, TE polarization). Note that $\beta_x < 0$ is omitted, because the input is even. (b, c, d) Spatial distribution of the real parts of the incident and reflected signals for the respective excitations of Fig. 6(a). (b) $\gamma = 0.001/\lambda^2$, (c) $\gamma = 0.01/\lambda^2$ and (d) $\gamma = 0.1/\lambda^2$. Plot parameters: $\varepsilon = 3$, $U = 20$, $D = 5\lambda$.

I will consider three signals like the ones of (22) with different γ values, whose Fourier transforms (23) are represented in Fig. 6(a) with respect to β_x/k. The vertical dashed lines denote the part of the spectrum $k_0 < \beta_x < k$, which is perfectly reflected, namely, the involved waves become evanescent into vacuum despite being originally propagating.

Note that the depicted quantity is an even function of β_x and, thus, it is plotted only for $\beta_x > 0$. It is clear that when γ gets smaller, the signal in the Fourier domain concentrates around a specific $\beta_x \cong \pm\kappa$ and, accordingly, resembles a non-causal harmonic tone along x-axis. This case is examined in Fig. 6(b) (the smallest value of $\gamma = 0.001/\lambda^2$), where the input waveform is spread over many wavelengths, decaying reluctantly from $x = 0$. The (real part of) reflective output also oscillates over a large part of x-axis, but with its magnitude increasing away from the origin, indicating a different local spatial distribution across the front interface of the device, compared to the excitation.

In Fig. 6(c), a higher value of γ is regarded and the operation of the setup as a spatial splitter is more directly demonstrated. Indeed, the system is fed by a single Gaussian pulse, but outputs two pulses with a considerable physical separation. Note that the reflected field occupies two continuous bands of spatial frequencies β_x (with nonzero size, unlike delta functions in the examples of Fig. 5), each of which contributes with a different phase via the reflection coefficients $R(\arccos(\beta_x/k))$. These phase shifts result in a spatial translation in either positive or negative x-direction depending on whether $\beta_x > 0$ or $\beta_x < 0$, respectively. It is stressed that the gap between the reflected pulses increases for larger γ, because the signals are more spatially concentrated around their symmetry axes. This is further exemplified in Fig. 6(d), where the response to the input (22) is plotted for the case of largest $\gamma = 0.1/\lambda^2$. Such a spatial redistribution of propagated power can be exploited in phased arrays applications, where reduction of grating lobes [41], reconfigurable beamforming [42] and directional gain enhancement [43] are typical aims.

3.5 Spatial Shifting

To further examine the physical shift of the reflection peak, consider the signal (22), where the real harmonic tone is replaced by its complex exponential: $F_{\text{inc}} = \sqrt[4]{\gamma\lambda^2}\, e^{-\gamma x^2} e^{\mathrm{i}\kappa x}$. The spatial Fourier transform of this signal is similar to the one given by (23) except that it consists of only one Gaussian. In other words, the Fourier transforms, unlike those of signals in Fig.6(a), are indeed unilateral and only nonzero for $\beta_x > 0$. In Fig. 7(a), I plot the transform for three inputs with different κ values; clearly, the inputs with small κ are only partially reflected since the portion of the signal with $\beta_x < k_0$ is almost perfectly transmitted. The latter scenario is illustrated in Fig. 7(b) (the smallest $\kappa = 6/\lambda$), where the reflected signal is substantially suppressed compared to the incoming one. On the contrary, when only a small portion of the input is transmitted ($\kappa = 7/\lambda$, Fig. 7(c)), the reflection looks similar to the original pulse, but with a lower peak and, overall, a wider profile. Finally, as depicted in Fig. 7(d) ($\kappa = 8/\lambda$), if the input pulse is within the interval $k_0 < \beta_x < k$, then the reflected signal is almost an exact copy of the incoming one.

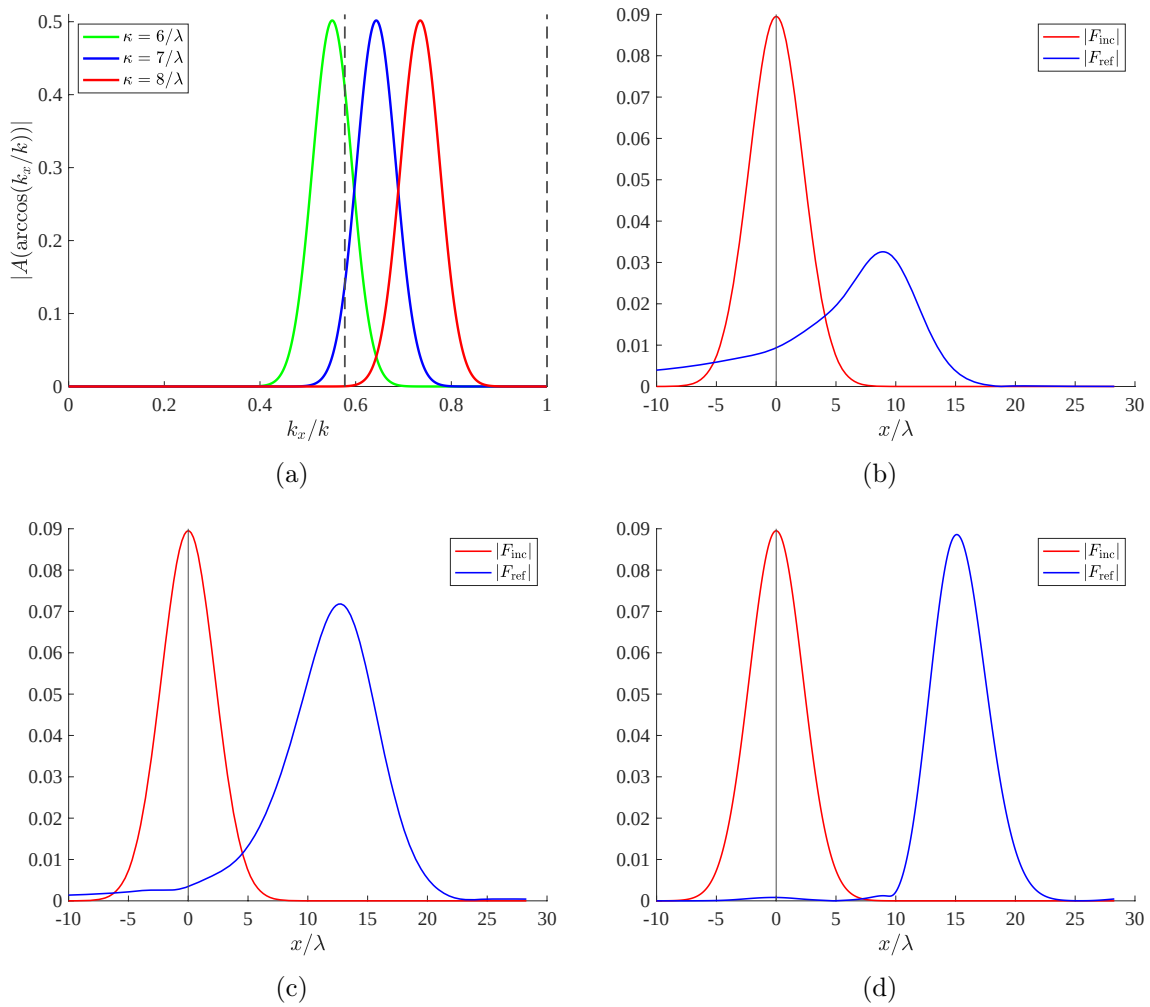

Figure 7: (a) Magnitude of spectral Fourier transform of complex modulated Gaussian pulses centered around different values of $\beta_x = \kappa$, serving as incoming signals ($z = 0$, TE polarization). (b, c, d) Spatial distribution of the magnitudes of the incident and reflected signals for the respective excitations of Fig. 7(a). (b) $\kappa = 6/\lambda$, (c) $\kappa = 7/\lambda$ and (d) $\kappa = 8/\lambda$.

In all the examined examples, the reflection peak is physically shifted with respect to the original one, which can be explained by referring to the Goos-Hänchen effect [44]. The considered input can be decomposed into a set of waves incident at different angles θ with the major propagation direction dictated by κ. Due to the slight variation in θ, the incoming waves are reflected with phase differences, which result in an interference pattern being observed. Due to the finite aperture of the incoming beam, one does not record standing waves originating from the superposition of the reflected components, but rather a spatial translation of the magnitude peak. Therefore, the proposed setup can also be used as an efficient reflective beam shifter in sensing and switching applications. This is demonstrated in Fig. 8(b), where the direction of the propagation of a beam emitted by an aperture radiator is altered using the proposed structure. The reflected beam remains largely focused with only little dispersion. Note that, as depicted in Fig. 8(a), if the number of layers is insufficient, then the emitted beam will disperse upon

reflection creating an interference pattern.

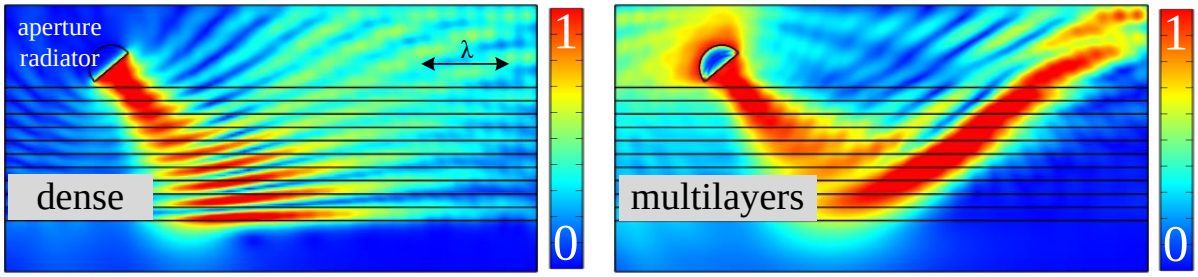

(a) (b)

Figure 8: Electric field spatial distribution Ey under excitation from an aperture radiator. (a) The area $0 < z < D$ is filled with dense material of the permittivity ε. The interference pattern is observed due to the Goos-Hänchen effect. (b) The area $0 < z < D$ is filled with graded-index multilayers. Only small dispersion in the reflected beam is observed. Simulation parameters: $\varepsilon = 50$, $U = 10$, $D = 0.1\lambda$, TE polarization.

Another potential utility of the proposed multilayered structure concern the interaction of filtered waves with components that are located into free space. In Fig. 9, I consider a line source into the dense medium, in the presence of a two-dimensional, near-field scatterer of arbitrary shape and examine three scenarios: when the area $0 < z < D$ is empty (left panel), when it is filled with a dense material of permittivity ε (central panel) and when it is replaced by the optimal graded-index multilayers (right panel).

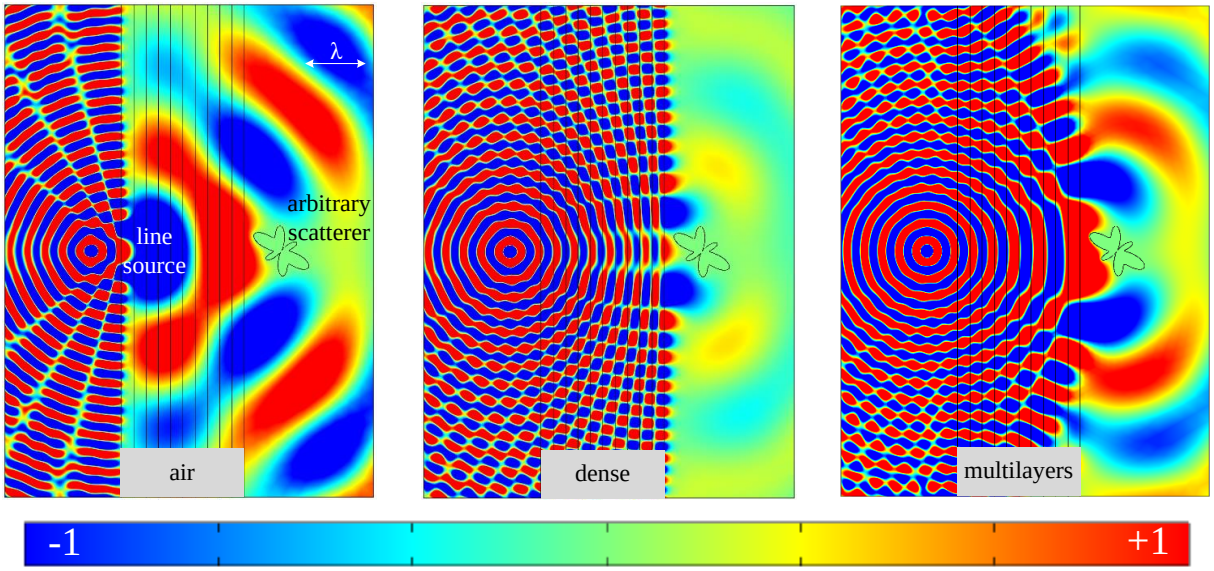

Figure 9: Electric field spatial distribution Ey under line source excitation from the front side and an arbitrary-shaped impenetrable scatterer near the rear interface. In the left panel, the intermediate region is filled with air, in the middle one, it is filled with dense medium and, in the right one, it is filled with the proposed graded-index multilayers. Simulation parameters: $\varepsilon = 50$, $U = 10$, $D = 0.1\lambda$, TE polarization.

In the left panel, I record huge reflections due to the small distance of the antenna from the abrupt interface, accompanied by strong diffusion of the signal into the free space that gets substantially perturbed by the scatterer. In the central panel, the reflections are mitigated but, at the same time, very low percentage of the incident power leaks to interact with the external component; therefore, the textural discontinuity isolates the scatterer from the dense medium. However, when the graded-index multilayers are employed, the reflections are almost negligible, while the diffused field "engulfs" the near-field object admitting it to exchange energy with the region of dielectric constant ε as if the material contrast is absent. Note that the incoming illumination penetrates through the slabs and goes around the scatterer so that the field isophase lines are closed and maximize its object-source engagement, unlike in the left panel.

Noticeably, the multilayered device can be paired with suitable gratings operated as arrays of optical switches or modulators for use in advanced optical signal processing and communication systems [45]. Similarly, the angular filtering with the proposed structure may work under an electromagnetic bandgap created by a row of defect rods achieving polarization isolation [46]. It should be stressed that all of the investigated examples were TE polarized, but the obtained results would be qualitatively identical if the inputs were TM waves. The reason is that the portion of the spectrum $|\beta_x| > k_0$ is totally reflected, while the remaining part with $|\beta_x| < k_0$ is almost fully transmitted, regardless of the polarization of the input. So, the reflected waveform is dictated only by the spatial distribution of the incident signal without much regard to the polarization (TE/TM).

3.6 Dissipation Effect

All of the previous designs were of lossless nature, since dense dielectrics with negligible thermal effects can be easily found. However, it would be interesting to identify the influence of a loss tangent in the intermediate layers $u = 1, \cdots, U$. In particular, let us assume equal relative losses for each of them, namely, $\mathrm{Im}[\varepsilon_u] = -\mathrm{Re}[\varepsilon_u] \tan\delta$; that results in the exponential decay of the amplitude of the propagating waves across the interior of the device, which effectively blurs the distinction between purely propagating and purely evanescent signals. It is noteworthy that the introduction of losses affects negatively both of the terms in the metric (21): for waves incident at angles $\theta < \theta_c$, larger reflections occur at $z = 0$, because of the abrupt transition from the lossless incoming medium ($\mathrm{Im}[\varepsilon] = 0$) to the lossy first layer ($\mathrm{Im}[\varepsilon_1] \cong -\varepsilon \tan\delta$). As for the waves incident at $\theta > \theta_c$, they will be partially absorbed not only into the layers that were propagative, but also into these that were evanescent in the lossless case ($\tan\delta = 0$).

In Fig. 10, the performance $1/\rho$, as defined by (21), is plotted as a function of the loss tangent $\tan\delta > 0$ and total optical thickness D/λ; note that due to losses the second term in equation (21) is not zero anymore. In Fig. 10(a), where the TE-polarized input is considered, a strong deterioration in the achieved score is recorded for increasing losses since a considerable amount of input power dissipates. When it comes to the optical size of

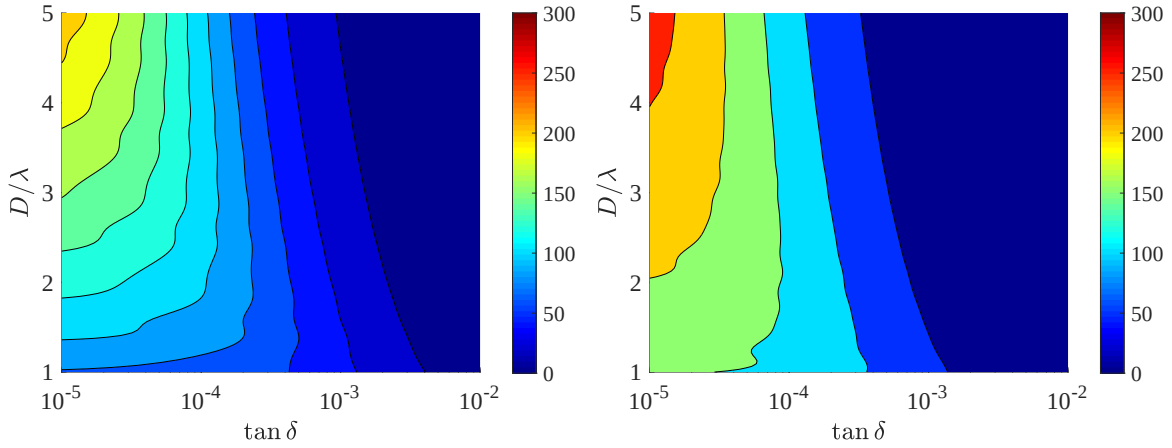

(a) (b)

Figure 10: Performance $1/\rho$ as a function of $\tan\delta$ and the total thickness of the device D/λ, in the cases of: (a) TE waves, (b) TM waves. Incidence of unitary magnitude is considered. Plot parameters: $\varepsilon = 3$, $U = 30$.

the device D/λ, it renders the filter more efficient due to the smoother textural transition as indicated by Fig. 3 and 4; on the other hand, a thicker design leads to more substantial thermal losses as seen from the performance minimum in the top right corner. Similarly, in Fig. 10(b) (TM polarization), the same thermal conversion is observed; nevertheless, in the low-loss region, a higher performance is noticed for the TE polarized input, which is in agreement with the trends presented in the lossless scenario of Fig. 3.

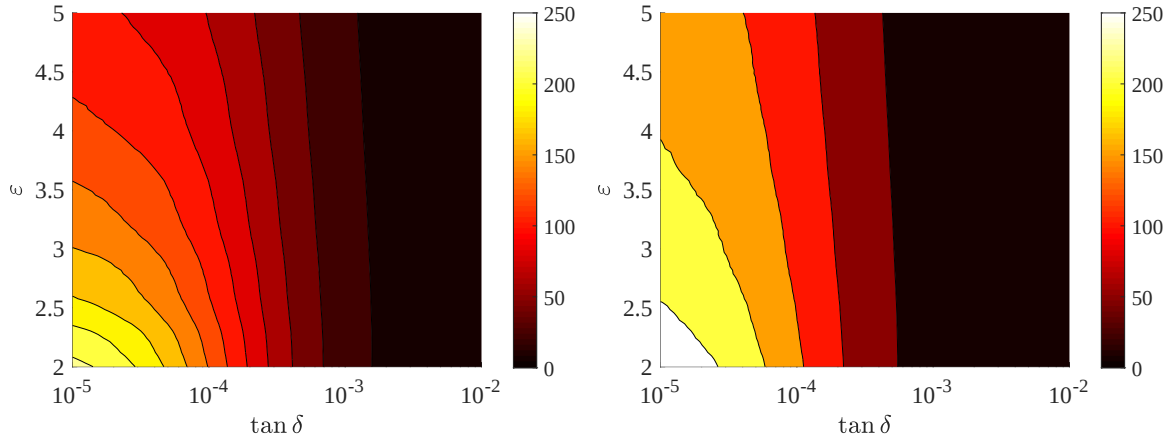

(a) (b)

Figure 11: Performance $1/\rho$ as a function of $\tan\delta$ and the maximal permittivity ε, in the cases of: (a) TE waves, (b) TM waves. Incidence of unitary magnitude is considered. Plot parameters: $U = 30$, $D/\lambda = 3$.

In Fig. 11(a), I consider a TE-polarized input and represent the metric $1/\rho$ as a function of the loss tangent $\tan\delta > 0$ and the permittivity of the incidence medium ε. As in the lossless case in Fig. 4, the highest performance is recorded for the smallest ε due

to the decreased material discontinuity across the proposed setup. When the tangent loss increases, the performance drops more rapidly for larger ε since the intermediate relative permittivities acquire more significant imaginary parts. Similar conclusions can be drawn by examining Fig. 11(b), where the decline of $1/\rho$ is even more abrupt both with respect to $\tan\delta$ and ε due to the adopted TM polarization.

CONCLUSION

Designs for angular filtering, based on a multilayered structure with increasingly sparser dielectric slabs, have been proposed. Due to total internal reflection, the portion of the spectrum with high spatial frequency is reflected in its entirety, contrary to the remaining portion which is subjected to almost perfect transmission because of the smooth permittivity change. The sharpness of the filter has been tested against the number of layers, the total optical thickness and the permittivity of the incidence medium; it seems that the separation between the two bands remains clear even in the presence of substantial dissipation. Once the proposed configuration gets supplied with a modulated Gaussian signal, it physically splits the single pulse into two identical ones with smaller amplitude; alternatively, the device can spatially shift the maximum of the pulse, as dictated by the Goos-Hänchen effect. Thus, the proposed ultra-sharp responses can be employed in numerous photonic operations from power splitting and beam shifting to suppression of sidelobes and low-profile interactions with near-field scatterers.

Seeing the recent advances in miniaturizing the optical devices through metamaterials, one can attempt to modify the proposed filter by assuming the incidence medium to be vacuum and using multilayers terminated by epsilon-near-zero and lossier substances. Another meaningful expansion of this work would be to examine alternative utilities for similar structures by perturbing the permittivities of the used media in a non-linear fashion, so that the emerging bandgaps lead to selective filtering across several bands. Importantly, manipulation of evanescent modes can be performed with a related setup by involving thin plasmonic layers supporting negative refraction. The permittivities of each layer can make a multi-dimensional parametric space into which the, properly defined, performance of the considered planar filter can be maximized accordingly. Due to the inherent complexity of these optimization problems, deep learning techniques assisted by artificial neural networks can be utilized in direct analogy to nanophotonic designs of multilayered scatterers [47, 48].

REFERENCES

[1] J. C. Maxwell, "On the general laws of optical instruments," in *The Scientific Papers of James Clerk Maxwell*, Vol. 1, edited by W. D. Niven (Cambridge Univ. Press, Cambridge, UK, 2011) p. 271–285.

[2] T. Smith, "On perfect optical instruments," Proc. Phys. Soc. **60**, 293 (1948).

[3] R. Luneburg, *Mathematical Theory of Optics* (Univ. of California Press, Berkeley, CA, USA, 2021).

[4] J. B. Pendry, "Negative refraction makes a perfect lens," Phys. Rev. Lett. **85**, 3966 (2000).

[5] J. B. Pendry, D. Schurig, and D. R. Smith, "Controlling electromagnetic fields," Science **312**, 1780 (2006).

[6] A. Alù, M. G. Silveirinha, A. Salandrino, and N. Engheta, "Epsilon-near-zero metamaterials and electromagnetic sources: Tailoring the radiation phase pattern," Phys. Rev. B **75**, 155410 (2007).

[7] N. Yu and F. Capasso, "Flat optics with designer metasurfaces," Nat. Mater. **13**, 139 (2014).

[8] A. Silva, F. Monticone, G. Castaldi, V. Galdi, A. Alù, and N. Engheta, "Performing mathematical operations with metamaterials," Science **343**, 160 (2014).

[9] N. M. Estakhri, B. Edwards, and N. Engheta, "Inverse-designed metastructures that solve equations," Science **363**, 1333 (2019).

[10] D. C. Tzarouchis, M. J. Mencagli, B. Edwards, and N. Engheta, "Mathematical operations and equation solving with reconfigurable metadevices," Light: Sci. Appl. **11**, 263 (2022).

[11] A. Y. Piggott, J. Lu, K. G. Lagoudakis, J. Petykiewicz, T. M. Babinec, and J. Vučković, "Inverse design and demonstration of a compact and broadband on-chip wavelength demultiplexer," Nat. Photonics **9**, 374 (2015).

[12] Z. Wang, T. Li, A. Soman, D. Mao, T. Kananen, and T. Gu, "On-chip wavefront shaping with dielectric metasurface," Nat. Commun. **10**, 3547 (2019).

[13] Q. He, F. Zhang, M. Pu, X. Ma, X. Li, J. Jin, Y. Guo, and X. Luo, "Monolithic metasurface spatial differentiator enabled by asymmetric photonic spin-orbit interactions," Nanophotonics **10**, 741 (2021).

[14] C. Guo, H. Wang, and S. Fan, "Squeeze free space with nonlocal flat optics," Optica **7**, 1133 (2020).

[15] I. M. Vellekoop, A. Lagendijk, and A. P. Mosk, "Exploiting disorder for perfect focusing," Nat. Photonics **4**, 320 (2010).

[16] A. N. Papadimopoulos, A. Duspayev, N. L. Tsitsas, N. V. Kantartzis, and C. Valagiannopoulos, "Wavefront engineering with optimally loaded absorbing metamirrors," Phys. Rev. B **103**, 165307 (2021).

[17] A. Hurtado, R. Raghunathan, I. D. Henning, M. J. Adams, and L. F. Lester, "Simultaneous microwave- and millimeter-wave signal generation with a 1310-nm quantum-dot-distributed feedback laser," IEEE J. Sel. Top. Quantum Electron. **21**, 568 (2015).

[18] T. Knightley, A. Yakovlev, and V. Pacheco-Peña, "Neural network design of multilayer metamaterial for temporal differentiation," (2022), *arXiv:2207.07556*.

[19] A. M. Patel and A. Grbic, "Transformation electromagnetics devices based on printed-circuit tensor impedance surfaces," IEEE Trans. Microw. Theory Tech. **62**, 1102 (2014).

[20] T. J. Cui, M. Q. Qi, X. Wan, J. Zhao, and Q. Cheng, "Coding metamaterials, digital metamaterials and programmable metamaterials," Light: Sci. Appl. **3**, e218 (2014).

[21] J. A. Rodríguez, A. I. Abdalla, B. Wang, B. Lou, S. Fan, and M. A. Cappelli, "Inverse design of plasma metamaterial devices for optical computing," Phys. Rev. Appl. **16**, 014023 (2021).

[22] F. Monticone, N. M. Estakhri, and A. Alù, "Full control of nanoscale optical transmission with a composite metascreen," Phys. Rev. Lett. **110**, 203903 (2013).

[23] J. Gu, R. Singh, X. Liu, X. Zhang, Y. Ma, S. Zhang, S. A. Maier, Z. Tian, A. K. Azad, H.-T. Chen, *et al.*, "Active control of electromagnetically induced transparency analogue in terahertz metamaterials," Nat. Commun. **3**, 1 (2012).

[24] M. Khorasaninejad, W. T. Chen, R. C. Devlin, J. Oh, A. Y. Zhu, and F. Capasso, "Metalenses at visible wavelengths: Diffraction-limited focusing and subwavelength resolution imaging," Science **352**, 1190 (2016).

[25] DARPA, "Work begins on next generation of battlefield obscurants." (accessed Nov. 25, 2022).

[26] A. Wang, "Electrically tunable quasioptical filters enabled by inverse design of epsilon-near-zero metasurfaces." (accessed Nov. 25, 2022).

[27] "Meta Materials Inc." (accessed Nov. 25, 2022).

[28] "Tunoptix, Inc. tunoptix.com, Metalenz, Inc. metalenz.com, Oblate Optics, Inc. oblateoptics.com," (accessed Nov. 25, 2022).

[29] A. E. Minovich, A. E. Miroshnichenko, A. Y. Bykov, T. V. Murzina, D. N. Neshev, and Y. S. Kivshar, "Functional and nonlinear optical metasurfaces," Laser Photonics Rev. **9**, 195 (2015).

[30] L. Li, H. Zhao, C. Liu, L. Li, and T. J. Cui, "Intelligent metasurfaces: Control, communication and computing," eLight **2**, 1 (2022).

[31] A. Arbabi, E. Arbabi, Y. Horie, S. M. Kamali, and A. Faraon, "Planar metasurface retroreflector," Nat. Photonics **11**, 415 (2017).

[32] H. Kwon, D. Sounas, A. Cordaro, A. Polman, and A. Alù, "Nonlocal metasurfaces for optical signal processing," Phys. Rev. Lett. **121**, 173004 (2018).

[33] J. Zhou, H. Qian, C.-F. Chen, J. Zhao, G. Li, Q. Wu, H. Luo, S. Wen, and Z. Liu, "Optical edge detection based on high-efficiency dielectric metasurface," Proc. Natl. Acad. Sci. **116**, 11137 (2019).

[34] H. Rajabalipanah, A. Momeni, M. Rahmanzadeh, A. Abdolali, and R. Fleury, "Parallel wave-based analog computing using metagratings," Nanophotonics **11**, 1561 (2022).

[35] A. Pors, M. G. Nielsen, and S. I. Bozhevolnyi, "Analog computing using reflective plasmonic metasurfaces," Nano Lett. **15**, 791 (2015).

[36] S. Gao, C. Zhou, W. Liu, W. Yue, S. Chen, S.-S. Lee, D.-Y. Choi, and Y. Li, "Dielectric polarization-filtering metasurface doublet for trifunctional control of full-space visible light," Laser Photonics Rev. **16**, 2100603 (2022).

[37] C. A. Valagiannopoulos, T. A. Tsiftsis, and V. Kovanis, "Metasurface-enabled interference mitigation in visible light communication architectures," J. Opt. **21**, 115702 (2019).

[38] C. Balanis, *Advanced Engineering Electromagnetics* (Wiley, Hoboken, NJ, USA, 2012).

[39] C. A. Valagiannopoulos, "Electromagnetic propagation into parallel-plate waveguide in the presence of a skew metallic surface," Electromagn. **31**, 593 (2011).

[40] C. A. Valagiannopoulos and N. L. Tsitsas, "Linearization of the T-matrix solution for quasi-homogeneous scatterers," J. Opt. Soc. Am. A **26**, 870 (2009).

[41] M. Bray, D. Werner, D. Boeringer, and D. Machuga, "Optimization of thinned aperiodic linear phased arrays using genetic algorithms to reduce grating lobes during scanning," IEEE Trans. Antennas Propag. **50**, 1732 (2002).

[42] J. Lau and S. Hum, "Reconfigurable transmitarray design approaches for beamforming applications," IEEE Trans. Antennas Propag. **60**, 5679 (2012).

[43] R. Gardelli, M. Albani, and F. Capolino, "Array thinning by using antennas in a Fabry–Perot cavity for gain enhancement," IEEE Trans. Antennas Propag. **54**, 1979 (2006).

[44] K. Bliokh and A. Aiello, "Goos-Hänchen and Imbert-Fedorov beam shifts: An overview," J. Opt. **15**, 014001 (2013).

[45] D. Rosenblatt, A. Sharon, and A. Friesem, "Resonant grating waveguide structures," IEEE J. Quantum Electron. **33**, 2038 (1997).

[46] Y. J. Lee, J. Yeo, R. Mittra, and W. S. Park, "Application of electromagnetic bandgap (EBG) superstrates with controllable defects for a class of patch antennas as spatial angular filters," IEEE Trans. Antennas Propag. **53**, 224 (2005).

[47] J. Peurifoy, Y. Shen, L. Jing, Y. Yang, F. Cano-Renteria, B. Delacy, J. Joannopoulos, M. Tegmark, and M. Soljačić, "Nanophotonic particle simulation and inverse design using artificial neural networks," Sci. Adv. **4**, eaar4206 (2018).

[48] A. Sheverdin, F. Monticone, and C. Valagiannopoulos, "Photonic inverse design with neural networks: The case of invisibility in the visible," Phys. Rev. Appl. **14**, 024054 (2020).